SCIENTIFIC REPORTS

OPEN

SUBJECT AREAS:
MICRO-OPTICS
OPTICS AND PHOTONICS

Received
20 August 2013

Accepted
27 January 2014

Published
12 February 2014

Correspondence and requests for materials should be addressed to K.K.M. (karanm@mit.edu)

* Current address: Intel Israel (74) LTD., Haifa, Israel.

High-Q CMOS-integrated photonic crystal microcavity devices

Karan K. Mehta[1], Jason S. Orcutt[1], Ofer Tehar-Zahav[2]*, Zvi Sternberg[2], Reha Bafrali[3], Roy Meade[4] & Rajeev J. Ram[1]

[1]Department of Electrical Engineering & Computer Science and Research Laboratory of Electronics, Massachusetts Institute of Technology, Cambridge, MA, USA 02139, [2]Micron Semiconductor Israel, Kiryat-Gat, Israel, [3]Micron Technology, Inc., Process R&D, San Jose, CA, USA 95134, [4]Micron Technology, Inc., Process R&D, Boise, ID, USA 83707.

Integrated optical resonators are necessary or beneficial in realizations of various functions in scaled photonic platforms, including filtering, modulation, and detection in classical communication systems, optical sensing, as well as addressing and control of solid state emitters for quantum technologies. Although photonic crystal (PhC) microresonators can be advantageous to the more commonly used microring devices due to the former's low mode volumes, fabrication of PhC cavities has typically relied on electron-beam lithography, which precludes integration with large-scale and reproducible CMOS fabrication. Here, we demonstrate wavelength-scale polycrystalline silicon (pSi) PhC microresonators with *Q*s up to 60,000 fabricated within a bulk CMOS process. Quasi-1D resonators in lateral p-i-n structures allow for resonant defect-state photodetection in all-silicon devices, exhibiting voltage-dependent quantum efficiencies in the range of a few 10 s of %, few-GHz bandwidths, and low dark currents, in devices with loaded *Q*s in the range of 4,300–9,300; one device, for example, exhibited a loaded *Q* of 4,300, 25% quantum efficiency (corresponding to a responsivity of 0.31 A/W), 3 GHz bandwidth, and 30 nA dark current at a reverse bias of 30 V. This work demonstrates the possibility for practical integration of PhC microresonators with active electro-optic capability into large-scale silicon photonic systems.

Optical microresonators[1] enable or enhance a diverse set of functions in integrated optical systems, spanning filtering and routing[2], switching and modulation[3], control of light emission[4], photodetection, and sensing. Low-volume optical modes are advantageous for a variety of reasons in all of these applications; examples include smaller footprint for dense integration, greater sensitivity to local index perturbations for sensors, greater energy efficiency in tuning for modulation, lower capacitance devices, stronger nonlinear interactions, and coupling to light emitters such as quantum dots and atoms. As a result, due to their ability to support very high-quality-factor (Q) resonant optical modes with mode volumes on the order of $(\lambda/n)^3$ or less, PhCs have attracted interest from a broad range of fields in recent years[5–9]. Much progress has been made in the optimization and fabrication of such structures, but due to the ~100-nm feature sizes required for structures with photonic bandgaps in the optical or near-infrared, fabrication typically relies on electron-beam lithography. This has limited the practical use of PhC structures, since it precludes practical integration with large-scale photolithographically defined systems, and also makes challenging the creation of complex structures requiring multiple masks[9].

Although the possibility for photolithographically defined quasi-2D PhCs has been explored in the past[10,11], high-Q resonators proved difficult to achieve. Passive optical cavities with measured quality factors (and extracted intrinsic Qs) of approximately 3,000 (10,000)[12] and 2,200 (on the order of 100,000)[13] have been designed and fabricated in SOI CMOS processes, but the potential for reliably creating active electro-optical devices in electrically-contacted PhC cavities capable of Qs exceeding 10^5 in a scalable process has remained unexplored.

In this work, we demonstrate PhC microresonators with radiation-loss limited Qs well in excess of 10^5 and measured material loss-limited Qs up to 58,000, fabricated photolithographically within a scaled CMOS process in the same patternable polycrystalline silicon (pSi) layer as used for transistor gates. A 1.2 μm thick, patterned oxide beneath optical devices eliminates the need for undercuts or any post-fabrication processing. We introduce also a laterally electrically-contacted design for a quasi-1D resonator utilizing a patterned, partially etched silicon layer, and demonstrate electro-optic functionality in the form of defect-state photodetection in a resonant p-i-n structure which allows efficient photodetection at 1550 nm wavelengths in an all-silicon CMOS device. These results indicate the potential for high-Q PC resonators to achieve both passive and active optical functionalities in scaled photonic systems, in a way that can be straightforwardly integrated with sophisticated electronics[14]. The

work indicates the practicality of silicon PhC microcavity devices for application in the near term for silicon photonic interconnects[15–17] and more speculatively in the long term for integrated quantum photonic systems[18].

Results

A schematic chip cross section around the pSi layer in the process used is shown in Fig. 1(a), showing p- and n-mos transistors and doping profiles in the crystalline silicon substrate. Passive optical structures can be formed within the undoped pSi used as the transistor gates, and losses down to 6 dB/cm at 1550 have been previously reported in waveguides formed in this layer[19]. A partial etch step allows thin wings to sit adjacent to the waveguide cores, which can be doped and electrically contacted with metal vias which access three patternable copper wiring layers. A conformal silicon-nitride ($n \approx 2.0$) layer encloses the pSi, and fills the holes in these designs which are otherwise SiO_2-clad, resulting in a lower index contrast than the Si/air structures which have achieved the highest Q/V ratios.

A 193 nm photolithography process with 0.68 numerical aperture was used to define features in the pSi. 100-nm features transferred to a photoresist using such illumination can suffer significant optical proximity effects[10], and here an optical proximity correction (OPC) algorithm partially compensated for such effects in definition of the circular holes; Fig. 1(d) shows the OPC-generated mask pattern for a triangular lattice of circular holes, and an example SEM image of a 2D lattice fabricated, with 375 nm lattice constant. From a set of SEM images on devices with a variety of lattice constants (a) and hole radii, an approximately linear relation between specified and achieved hole radii was found that was independent of lattice constant, and was used to compensate for uniform lithographic bias in future designs in the same process. Holes with radii down to about 55 nm formed reliably.

A variety of previously studied PC microcavity designs would be suitable for integration here. Minimization of radiative loss into the cladding motivates choice of cavities with smooth, ideally Gaussian envelopes[5,20,21], and quasi-1D structures, relying on photonic band-gap confinement in only one direction, are particularly robust in moderate index-contrast environments[22]. The bulk of our devices relied on such cavities.

Quasi-1D resonators for operation near 1550 nm using a linear array of holes in a 225 nm-height pSi waveguide of width $\approx$ 450 nm were designed with a lattice constant a near 330 nm, based on the hole tapering scheme developed in[23]. Around the cavity center to either side, hole radii decrease linearly from $r = 0.33a$ to $r = 0.28a$; a set of "mirror" holes, all with $r = 0.28a$ are added to either side, the number of which controls the strength of coupling to the feeding bus waveguides[24]. In the dielectric environment here, these resonators achieve intrinsic (that is, with no coupling to the feeding waveguides) radiative Qs of over 2 million, as calculated with finite-difference time-domain (FDTD) simulations[25] without material loss.

To allow efficient electrical contact to the resonator without introducing large optical loss, thin $\approx$ 50 nm-thick pSi "wings" were

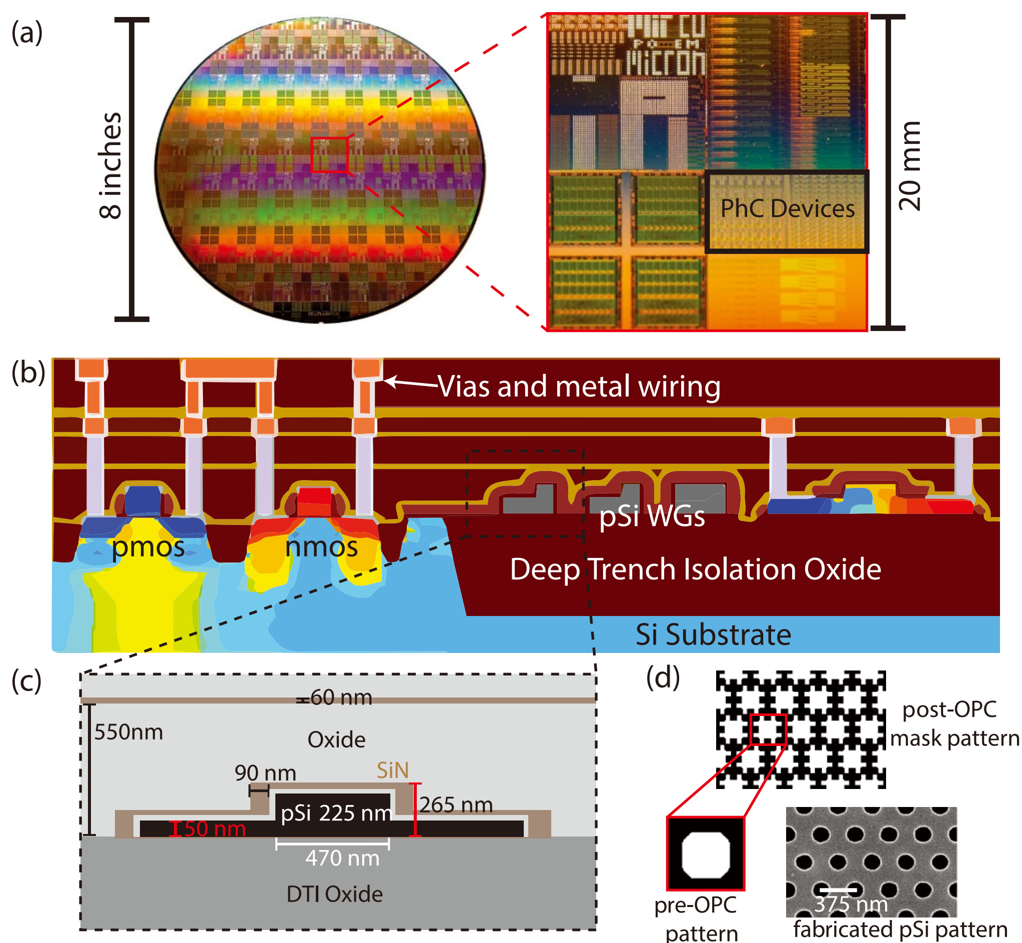

Figure 1 | (a) Photograph of full wafer, on which a single reticle (inset) was repeated. The location of the PhC devices discussed here is labeled within the inset. (b) Schematic chip cross-section (not to scale), illustrating (from left to right) doping profiles around nmos and pmos transistors with metal vias and copper wiring, intrinsic pSi waveguide structures separated from the silicon substrate by a 1.2 μm-thick Deep Trench Isolation (DTI) deposited oxide, and a doped and contacted electro-optic structure. (c) Detailed schematic including dimensions near optical cores. (d) Transformation of supplied (desired) pattern to mask design after optical proximity correction, and SEM images of 2D lattice of fabricated holes in pSi.

placed adjacent to the cavity. However, continuous slabs, in conjunction with the SiN liner layers, had effective indices large enough to couple to some Fourier components of the resonant mode, resulting in optical leakage, which could be reduced by patterning the wings with a 2D lattice of triangular low index holes; this had the effect also of reducing the resonant mode field's evanescent decay into the wings, allowing doped regions to be brought closer to the cavity (see Supplementary Information). This patterning was done with a lattice of $r = 0.3a$ holes here. An SEM image of a resulting structure along with the FDTD-calculated resonant electric field profile is shown in Fig. 2(b). The intrinsic radiative Q of the contacted structure was calculated to be $\approx 300{,}000$, and the mode volume $0.8(\lambda/n)^3$.

Light is coupled to independent devices via grating couplers from fibers oriented nearly normal to the chip surface; adiabatic tapers couple to the $\approx$ 500 nm-wide waveguides, as shown in the optical micrograph of Fig. 2(a). Transmission spectra through cavities with resonant wavelengths $\lambda_0 = 1510$ nm and $\lambda_0 = 1540$ nm, with three different waveguide coupling strengths (8, 12, and 18 pairs of mirror holes) are shown in Fig. 2(c) and (d), along with theoretical fits to Fano profiles[26] which allowed determination of each cavity's loaded quality factor. The peak transmissions of each cavity, measured and normalized to the grating coupler transmission loss calibrated separately, closely follow the theoretical prediction of a standard coupled mode analysis $T_{pk} = (Q_{tot}/Q_{WG})^2$ [27]. Here the total measured quality factor is related to the waveguide coupling strength via the relation $Q_{tot}^{-1} = Q_0^{-1} + Q_{WG}^{-1}$, where Q_0 is the cavity's intrinsic loss rate (due to material and radiative loss) and Q_{WG} is the quality factor associated only with the cavity loss rate into the bus WG modes. As shown in Fig. 2(e), the peak transmissions and measured total quality factors are closely fit by the theoretical prediction for intrinsic quality factors $Q_0 = 58{,}000$ and 51,000.

These loss rates are thus clearly limited not by the device design, but predominantly from material loss in the pSi and fabrication imperfections. Characterization of propagation loss in rectangular waveguides on the same wafer gives insight into the role of bulk material loss as well as sidewall roughness. The intensity loss coefficient of the bulk material in these samples is measured to be approximately $\alpha \approx 4$ dB/cm ≈ 0.92 cm^{-1}, corresponding to a temporal photon loss rate of $\gamma = \alpha c/n_{gr} \approx 8$ GHz, where n_{gr} is the waveguide group index. This results in a material loss-associated Q of $Q_{mat} = \omega/\gamma \approx 154{,}000$. However, sidewall roughness makes a significant contribution to loss in these devices as well. Rectangular waveguides of 400 nm width, in which the mode profile has significant overlap with the sidewalls, exhibited propagation losses of about 8.5 dB/cm at the wavelengths of interest. Although the overlap with the sidewalls in the PhC cavities can be expected to be only roughly that of the fundamental mode in the 400 nm rectangular waveguide, this measured loss would correspond to a total $Q_{mat\,+\,roughness} \approx 77{,}000$.

Variance in fabricated hole sizes could play a role as well; scattering loss has been resulted to scale approximately as $Q_{dis}^{-1} = A(\sigma_r/a)^2$, where σ_r represents the RMS radius deviation[28,29] and A represents a design and index-contrast-dependent parameter. Scanning electron microscope characterization of fabricated samples indicates $\sigma_r \approx 2.0$ nm, and FDTD simulations incorporating random disorder in the hole sizes with Gaussian distribution indicate $A \approx 0.1$ (see supplementary information), resulting in a $Q_{dis} \approx 280{,}000$. Together, these loss rates are consistent with the observed intrinsic Qs. Use of higher NA photolithography is known to allow lower sidewall roughness, and will likely improve disorder in the PhC features as well, which presents a clear path to reducing the impact of fabrication imperfections on these loss rates.

A significant fraction of the material loss (the dominant loss mechanism in these devices as discussed above) results from absorption events involving pSi grain boundary defect electronic states at energies within the bandgap[19,30]. Since such absorption events generate free carriers, a significant photocurrent may be expected to flow in the contacted diode structures, which should be observable under reverse bias. Such photodiode behavior has indeed been previously observed in pSi ridge waveguide ring resonator structures[31]; in crystalline silicon, such detection has been observed in samples with defects introduced by ion implantation with high responsivities of

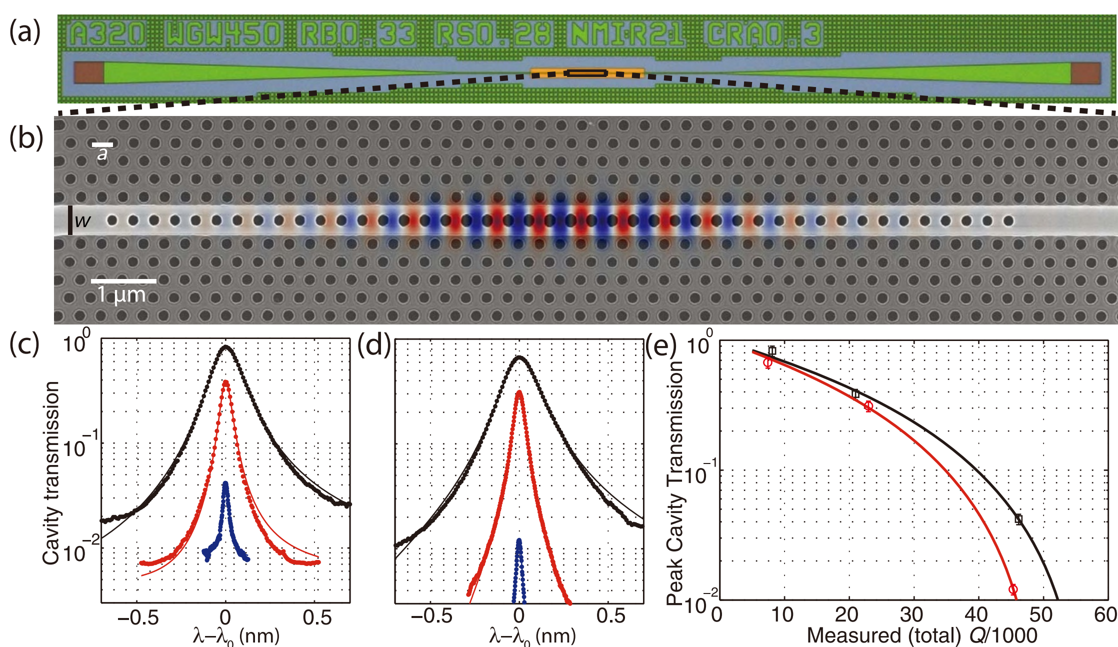

Figure 2 | (a) Optical micrograph of a single cavity device, with grating couplers and tapers for input/output light coupling. (b) SEM image of pSi in a fabricated PhC device, with FDTD-calculated mode profile overlaid. (c) and (d) Measured transmission spectra through cavities with resonant wavelengths $\lambda_0 \approx 1512$ ($a = 320$ nm, $w = 450$ nm) and $\lambda_0 \approx 1549$ nm ($a = 330$ nm, $w = 470$ nm), respectively. Curves and fits for cavities with 8, 12 and 18 pairs of mirror holes are shown for each (black, red and blue curves), with (e) peak resonant transmissions fit to theoretical predictions as function of total quality factor, allowing extraction of intrinsic Qs of 58,000 (black curve for $\lambda_0 = 1512$ nm cavity) and 51,000 (red curve, $\lambda_0 = 1549$ nm).

0.7 A/W[32] and even with avalanche gain allowing photodiode operation with 10 A/W operation and >35 GHz bandwidths[33]. Photodetection has been reported also in defects inherent at the Si/SiO_2 interfaces[34], and defect photogeneration mechanisms have been applied to resonant photodetectors as well[35,36].

A fabricated 1D PhC structure with lateral electrical contacts is shown in Fig. 3(a), with p+ and n+ doped regions shaded in red and blue. Variants were tested with doped region spacings of $w_i = 1.6\ \mu$m (structure and results shown in Fig. 3), as well as 1.0 and 2.2 μm. The cavity is coupled to a feeding waveguide from only one side, and ideally the loaded Q including coupling into the bus waveguide mode would be half that of the intrinsic Q, to ensure that no light is reflected into the bus, i.e. that the cavity is critically coupled[27]. In these devices, material loss in the pSi was higher due to additional processing steps, and devices had measured intrinsic Qs of approximately 22,000 with no p+/n+ regions nearby; the loaded Q of the resonator devices with $w_i = 1.0$, 1.6, and 2.2 μm were approximately 4,300, 8,000, and 9,300, respectively, indicating closeness to critical coupling for the larger intrinsic region widths and the effect of free-carrier absorption for the device with lowest w_i.

Dark current in the $w_i = 1.6\ \mu$m structure is below 500 pA at reverse biases up to 30 V (as shown in Fig. 3(b)), with large separation from the photocurrent when illuminated on resonance (near 1538 nm in this device) over a large voltage range. Photocurrent spectra obtained at a reverse bias of 22 V for input powers between 1 and 100 μW are plotted in Fig. 3(c); the carrier photogeneration rate is proportional to stored cavity energy, and the spectra are thus Lorentzian at low input powers and exhibit bistability resulting from the thermo-optic effect[37] at higher powers. The peak current relates directly to the onresonance quantum efficiency (QE), plotted over a range of input powers and biases in Fig. 3(d); QE here is defined as number of charge carriers extracted per photon incident on the cavity, calculated from $I_{pk}h\nu/P_{in}q$, where I_{pk} is the peak resonant photocurrent and P_{in} is the optical power input after the grating coupler. A strong voltage dependence is observed, and large voltages of at least 15 V are required to achieve QEs above 10%, likely due to inefficient extraction under low fields due to recombination in the 1.6 μm-wide intrinsic region. The power dependence of the peak QE appears similar to that previously reported in resonant pSi photodetectors[31], and could be due to density-dependent recombination rates; this effect must be stronger than any contribution from two-photon absorption at the higher powers in the range of powers studied here, since no increase in QE at high optical powers is observed. We applied a maximum of 30 V bias to the device, and observed a peak QE of 28% (0.35 A/W). At voltages in this range, material properties of the pSi appear to have been affected in a way which resulted in permanent (stable at least for many days) changes in the device response; the data presented here was verified to be stable, and we briefly discuss some of the changes observed in the Supplementary Information.

Geometry also strongly influenced the modulation response of the photodetectors. Devices with narrower intrinsic regions had significantly faster 3-dB bandwidths; a modulation response curve with an empirical fit is shown in Fig. 4(a) for a device with a 1 μm-wide intrinsic region with -30 V applied (a DC QE of 25% and 30 nA dark current were measured in this device and bias), indicating a 2.9 GHz 3-dB roll-off. Oscillations around the fit are repeatable and due primarily to impedance mismatch between the device's large series resistance and the 50 Ω load. The measured bandwidth increases strongly with increasing reverse bias, and is lower in devices with larger intrinsic region widths (the three curves in Fig. 4(b)). The device's RC limit is significantly higher than the measured roll-offs owing to its extremely small capacitance ($\epsilon A/d \approx 0.1$ fF), as is the RC limit owing to the load 50 Ω resistance and the contact pad

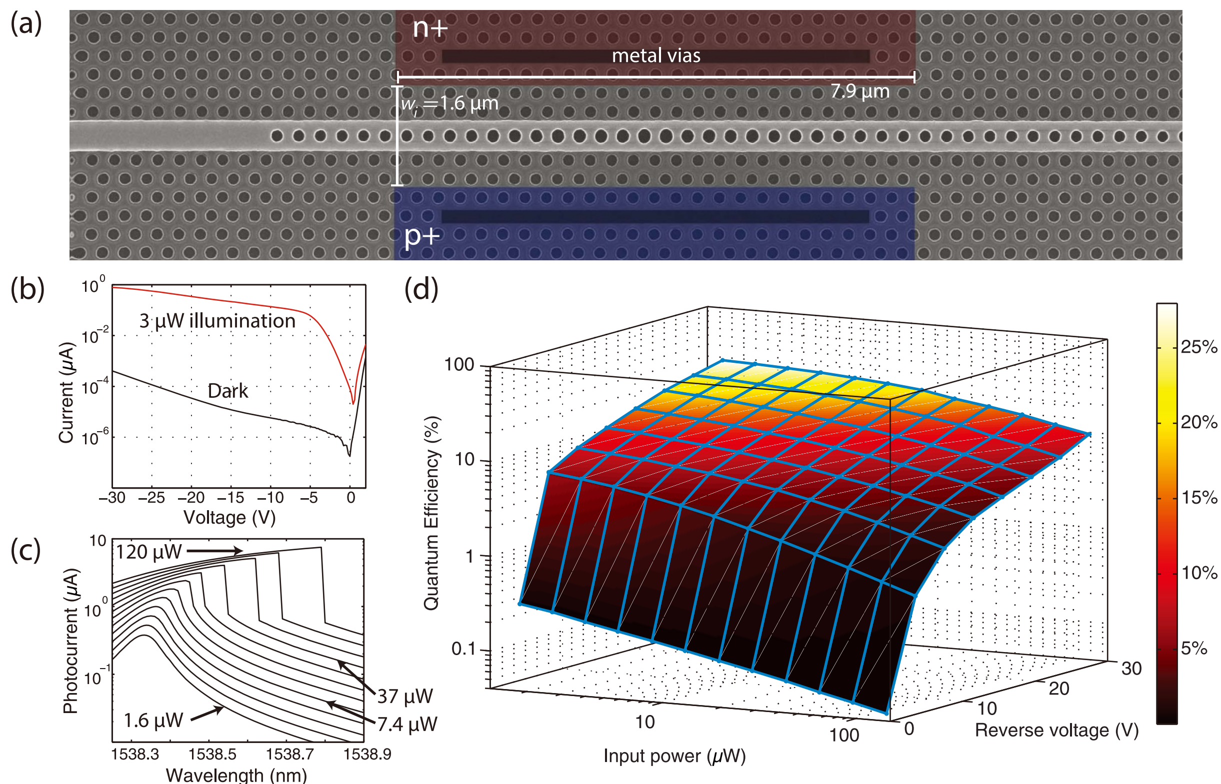

Figure 3 | (a) SEM image of detector structure with one optical input, with p+ and n+ implanted regions shaded. Measurements are presented in this figure for a device with intrinsic region width $w_i = 1.6\ \mu$m, as labeled. (b) IV characteristics without illumination and with 3 μW in-waveguide power at cavity resonance wavelength. (c) Photocurrent spectra at reverse bias of 22 V for powers logarithmically spaced between 1.6 and 120 μW input optical power, and (d) Peak QE vs. voltage and power for resonant pSi PhC defect-state photodetector.

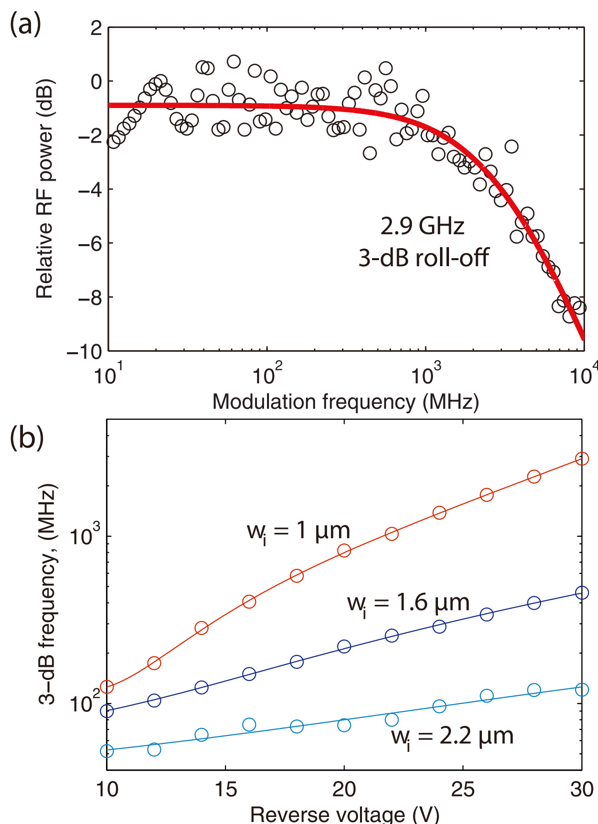

Figure 4 | (a) Modulation response of detector with 1 μm intrinsic region, under 30 V reverse bias with an empirical fit showing 2.9 GHz 3-dB frequency. DC quantum efficiency at this operating point was 25% (responsivity 0.31 A/W), with a dark current of 30 nA. (b) Fit 3-dB frequencies for 3 different devices with identical optical design, but different intrinsic region widths (w_i, as labeled; the middle curve shows results from the same device as in Fig. 3) as a function of applied reverse voltage. Lines are guides to the eye.

capacitance; the measured frequency responses are, however, plausibly explained in terms of the limit imposed by the transit time through the intrinsic region, which increases with intrinsic region width and varies inversely with mobility. Both electron and hole mobilities in pSi thin films are known to decrease with film thickness[38], consistent with the strong dependence on the width of the 50-nm partial etched wings the carriers have to traverse in these devices.

Discussion

Simple improvements to the electrical design of the photodetectors presented above should allow faster response, along with higher quantum efficiencies at lower applied biases. Incorporating mid-level doped regions in addition to the p+ and n+ used in these structures so as to form a p+/p/i/n/n+ structure with p and n regions extending closer to the device center would allow lower w_is without introducing excessive optical loss, and therefore higher transit time-limited bandwidths (inversely proportional to w_i); thicker contact wings would also increase bandwidth by increasing mobility in the wings. Both of these modifications would also be expected to reduce the applied voltages required for carrier extraction by reducing recombination in the intrinsic region.

The photodetector results presented above constitute a first realization of electrically active PhC devices in a CMOS environment, but together with the possibility for increased bandwidth and reduced operating voltage also indicate promise generally for resonant sub-bandgap photodetection with sub-nA dark currents and low capacitance in this environment. Use of higher NA photolithography in more modern processes should also allow for lower roughness and disorder-induced loss, and higher intrinsic Qs in PhC devices generally.

Our work demonstrates that pSi PhC microresonators with quality factors of up to 60,000 in passive devices can be designed and fabricated within a scaled CMOS foundry in the same layer as is used for transistor gates, with potential for significant improvement with process and material quality. The contacted designs and the photodetector device presented here also indicate the potential for active wavelength-scale electro-optic devices. In the context of integrated Si photonic interconnects, we expect these results could impact design considerations primarily for low-capacitance resonant photodetectors (both linear and nonlinear) and high-efficiency modulators. Quantum photonic applications relying on such resonators may eventually benefit as well from the ability to produce them in scaled processes, integrated tightly with control electronics and tuning mechanisms.

Methods

Cavity simulation and design. Design proceeded by first calculating band structures of 1D PhC waveguides[39] to approximately locate parameters for the desired resonant frequency, after which FDTD simulation in MEEP[25] of the full design allowed for quality factor calculation and optimization. Band structures of the 2D contact slab, as shown in the supplementary information, were calculated with the same method as for the 1D cavity waveguides. Designed devices were laid out within Cadence Design Systems' Virtuoso, a common VLSI layout tool[40].

Device characterization. An HP 8164A lightwave measurement system was used for spectral measurements; the laser linewidth (and hence spectral resolution) is $<$ 1 MHz. An Agilent 4156C semiconductor parameter analyzer was used for DC biasing and current measurement. For modulation response measurements, the output of a microwave synthesizer was modulated onto the input light with a lithium niobate modulator, and the RF power in the device photocurrent measured with a microwave spectrum analyzer. Consideration of the RF power measured in the PhC device relative to that under the same measurement performed on a commercial photodiode with a frequency response known to be flat (Discovery Semiconductor DSC20S) for frequencies up to 20 GHz allows for elimination of any frequency response from components in the system other than the PhC device.

1. Vahala, K. J. Optical microcavities. *Nature* **424**, 839–846 (2003).
2. Little, B. E., Chu, S. T., Haus, H. A., Foresi, J. & Laine, J.-P. Microring resonator channel dropping filters. *IEEE J. Lightwave Tech.* **15**, 998–1005 (1997).
3. Xu, Q., Schmidt, B., Pradhan, S. & Lipson, M. Micrometre-scale silicon electro-optic modulator. *Nature* **435**, 325–327 (2005).
4. Noda, S., Fujita, M. & Asano, T. Spontaneous-emission control by photonic crystals and nanocavities. *Nature Photon.* **1**, 449–458 (2007).
5. Akahane, Y., Asano, T., Song, B.-S. & Noda, S. High-Q photonic nanocavity in a two-dimensional photonic crystal. *Nature* **425**, 944–947 (2003).
6. Englund, D. *et al.* Controlling the spontaneous emission rate of single quantum dots in a two-dimensional photonic crystal. *Phys. Rev. Lett.* **95**, 013904 (2005).
7. Vlasov, Y. A., O'Boyle, M., Hamann, H. F. & McNab, S. J. Active control of slow light on a chip with photonic crystal waveguides. *Nature* **438**, 65–69 (2005).
8. Soljačić, M. & Joannopoulos, J. Enhancement of nonlinear effects using photonic crystals. *Nature Mater.* **3**, 211–219 (2004).
9. Ellis, B. *et al.* Ultralow-threshold electrically pumped quantum-dot photonic-crystal nanocavity laser. *Nature Photon.* **5**, 297–300 (2011).
10. Selvaraja, S. K. *et al.* Fabrication of photonic wire and crystal circuits in silicon-on-insulator using 193-nm optical lithography. *IEEE J. Lightwave Tech.* **27**, 4076–4083 (2009).
11. Bogaerts, W. *et al.* Nanophotonic waveguides in silicon-on-insulator fabricated with CMOS technology. *IEEE J. Lightwave Tech.* **23**, 401–412 (2005).
12. Schelew, E., Rieger, G. W. & Young, J. F. Characterization of integrated planar photonic crystal circuits fabricated by a CMOS foundry. *IEEE J. Lightwave Tech.* **31**, 239–248 (2013).
13. Poulton, C. V. *et al.* Linear photonic crystal microcavities in zero-change SOI CMOS. ITA5A.6 (Optical Society of America, Rio Grande, Puerto Rico, United States, 2013).
14. Georgas, M., Orcutt, J., Ram, R. J. & Stojanovic, V. A monolithically-integrated optical receiver in standard 45-nm SOI. *IEEE J. Solid State Circ.* **47**, 1693–1702 (2012).
15. Batten, C. *et al.* Building many-core processor-to-DRAM networks with monolithic CMOS silicon photonics. *IEEE Micro* **29**, 8–21 (2009).
16. Orcutt, J. S. *et al.* Open foundry platform for high-performance electronic-photonic integration. *Optics Exp.* **20**, 12222–12232 (2012).
17. Hochberg, M. & Baehr-Jones, T. Towards fabless silicon photonics. *Nature Photon.* **4**, 492–494 (2010).

18. Faraon, A. *et al.* Integrated quantum optical networks based on quantum dots and photonic crystals. *New J. Phys.* **13**, 055025 (2011).
19. Orcutt, J. S. *et al.* Low-loss polysilicon waveguides fabricated in an emulated high-volume electronics process. *Opt. Express* **20**, 7243–7254 (2012).
20. Srinivasan, K. & Painter, O. Momentum space design of high-Q photonic crystal optical cavities. *Optics Exp.* **10**, 670–684 (2002).
21. Kuramochi, E. *et al.* Ultrahigh-high Q photonic crystal nanocavities realized by the local width modulation of a line defect. *Appl. Phys. Lett.* **88**, 041112–041112 (2006).
22. Quan, Q., Burgess, I. B., Tang, S. K. Y., Floyd, D. L. & Loncar, M. High-Q, low index-contrast polymeric photonic crystal nanobeam cavities. *Optics Exp.* **19**, 22191–22197 (2011).
23. Quan, Q. & Loncar, M. Deterministic design of wavelength scale, ultra-high Q photonic crystal nanobeam cavities. *Optics Exp.* **19**, 18529–18542 (2011).
24. Quan, Q., Deotare, P. B. & Loncar, M. Photonic crystal nanobeam cavity strongly coupled to the feeding waveguide. *Appl. Phys. Lett.* **96**, 203102–203102 (2010).
25. Oskooi, A. F. *et al.* MEEP: A flexible free-software package for electromagnetic simulations by the FDTD method. *Comp. Phys. Comm.* **181**, 687–702 (2010).
26. Mehta, K. K., Orcutt, J. S. & Ram, R. J. Fano line shapes in transmission spectra of silicon photonic crystal resonators. *Appl. Phys. Lett.* **102**, 081109 (2013).
27. Haus, H. A. *Waves and fields in optoelectronics* (Prentice-Hall, Englewood Cliffs, NJ, 1984).
28. Gerace, D. & Andreani, L. C. Effects of disorder on propagation losses and cavity Q-factors in photonic crystal slabs. *Photonics and Nanostructures – fundamentals and applications* **3**, 120–128 (2005).
29. Galli, M. *et al.* Light scattering and Fano resonances in high-Q photonic crystal nanocavities. *Appl. Phys. Lett.* **94**, 071101–071101 (2009).
30. Jackson, W. B., Johnson, N. & Biegelsen, D. Density of gap states of silicon grain boundaries determined by optical absorption. *Appl. Phys. Lett.* **43**, 195–197 (1983).
31. Preston, K., Lee, Y. H. D., Zhang, M. & Lipson, M. Waveguide-integrated telecom-wavelength photodiode in deposited silicon. *Opt. Lett.* **36**, 52–54 (2011).
32. Geis, M. *et al.* All silicon infrared photodiodes: photo response and effects of processing temperature. *Optics Exp.* **15**, 16886–16895 (2007).
33. Geis, M. *et al.* Silicon waveguide infrared photodiodes with >35 GHz bandwidth and phototransistors with 50 AW^{-1} response. *Optics Exp.* **17**, 5193–5204 (2009).
34. Baehr-Jones, T., Hochberg, M. & Scherer, A. Photodetection in silicon beyond the band edge with surface states. *Optics Exp.* **16**, 1659–1668 (2008).
35. Doylend, J., Jessop, P. & Knights, A. Silicon photonic resonator-enhanced defect-mediated photodiode for sub-bandgap detection. *Optics Exp.* **18**, 14671–14678 (2010).
36. Yu, H. *et al.* Using carrier-depletion silicon modulators for optical power monitoring. *Opt. Lett.* **37**, 4681–4683 (2012).
37. Barclay, P. E., Srinivasan, K. & Painter, O. Nonlinear response of silicon photonic crystal microresonators excited via an integrated waveguide and fiber taper. *Optics Exp.* **13**, 801–820 (2005).
38. Kamins, T. Hall mobility in chemically deposited polycrystalline silicon. *J. Appl. Phys.* **42**, 4357–4365 (1971).
39. Johnson, S. G. & Joannopoulos, J. D. Block-iterative frequency-domain methods for maxwell's equations in a planewave basis. *Optics Exp.* **8**, 173–190 (2001).
40. Orcutt, J. S. & Ram, R. J. Photonic device layout within the foundry CMOS design environment. *IEEE Phot. Tech. Lett.* **22**, 544–546 (2010).

Acknowledgments

This work was carried out under the DARPA POEM program, managed by Dr. Jagdeep Shah. K. Mehta acknowledges support from a DOE Science Graduate Fellowship. The views expressed are those of the author and do not reflect the official policy or position of the Department of Defense or the U.S. Government. Approved for Public Release, Distribution Unlimited.

Author contributions

K.K.M. designed, laid out mask designs for and performed experiments on devices; J.S.O. established CAD layout infrastructure and coordinated full chip tapeout; O.T.-Z., Z.S., R.B. and R.M. handled optical proximity correction, CMOS process control, and fabrication; K.K.M. and R.J.R. prepared the manuscript, and all authors reviewed it; and R.J.R. supervised the research.

Additional information

Supplementary information accompanies this paper at http://www.nature.com/scientificreports

Competing financial interests: The authors declare no competing financial interests.

How to cite this article: Mehta, K.K. *et al.* High-*Q* CMOS-integrated photonic crystal microcavity devices. *Sci. Rep.* **4**, 4077; DOI:10.1038/srep04077 (2014).

This work is licensed under a Creative Commons Attribution-NonCommercial-ShareAlike 3.0 Unported license. To view a copy of this license, visit http://creativecommons.org/licenses/by-nc-sa/3.0